

# Persistence Images: An Alternative Persistent Homology Representation

Sofya Chepushtanova<sup>1</sup>, Tegan Emerson<sup>1</sup>, Eric Hanson<sup>1</sup>, Michael Kirby<sup>1</sup>, Francis Motta<sup>3</sup>,  
Rachel Neville<sup>1</sup>, Chris Peterson<sup>1</sup>, Patrick Shipman<sup>1</sup>, and Lori Ziegelmeier<sup>2</sup>

<sup>1</sup>Department of Mathematics, Colorado State University

<sup>2</sup>Department of Mathematics, Statistics, and Computer Science, Macalester College

<sup>3</sup>Department of Mathematics, Duke University

## Abstract

*Many datasets can be viewed as a noisy sampling of an underlying topological space. Topological data analysis aims to understand and exploit this underlying structure for the purpose of knowledge discovery. A fundamental tool of the discipline is persistent homology, which captures underlying data-driven, scale-dependent homological information. A representation in a "persistence diagram" concisely summarizes this information. By giving the space of persistence diagrams a metric structure, a class of effective machine learning techniques can be applied. We modify the persistence diagram to a "persistence image" in a manner that allows the use of a wider set of distance measures and extends the list of tools from machine learning which can be utilized. It is shown that several machine learning techniques, applied to persistence images for classification tasks, yield high accuracy rates on multiple data sets. Furthermore, these same machine learning techniques fare better when applied to persistence images than when applied to persistence diagrams. We discuss sensitivity of the classification accuracy to the parameters associated to the approach. An application of persistence image based classification to a data set arising from applied dynamical systems is presented to further illustrate.*

## 1 Introduction

In recent years, the field of topology has grown to include a large set of computational tools [1]. One of the fundamental tools is persistent homology. Given a nested sequence of topological spaces  $X_1 \subseteq X_2 \subseteq \dots \subseteq X_n$  the inclusion  $X_i \subseteq X_j$  for  $i < j$  induces a linear map on the corresponding  $k^{\text{th}}$  homology  $H_k(X_i) \rightarrow H_k(X_j)$ . Following an element of  $H_k(X_i)$  as the scale parameter (or "time") increases to a larger  $j$  is roughly the notion of persistence. The scale at which an element first appears in a homology group and the scale at which it disappears are called the *birth index*  $x$  and *death index*  $y$  respectively (under reasonable assumptions, these indices are computable, see § 2). Typically, persistent homology information is presented in one of two ways: a *Barcode* [2] or a *Persistence Diagram (PD)* [1].

The advent of *computational topology* has brought considerable interest in applying these tools to the analysis of data, which has become an area of research in its own right, *topological data analysis*. The presence of topological structures in data can be used to understand the landscape and ambient space in which a data set exists as well as to compare different data sets. Topological approaches to understanding data have been used in a variety of applications, for example, image webs, signal analysis, neuroscience, and biological aggregations [3, 4, 5, 6, 7, 8].

Concurrent to this revolution in topology, a growing general interest in data analysis has driven continued interest in data mining, pattern recognition, and machine learning (ML). Yet, the overlap between these data analysis techniques and TDA has been limited. For example, the insights of [9] have allowed a select set of ML tasks based on PDs. However, there is still not a concrete answer to how and when the tools of computational topology and machine learning should be used together. We provide one answer to this fundamental problem through a novel representation of a PD, which we call a *persistence image (PI)*.

A PI is derived from a mapping of a PD to an integrable function  $f : \mathbb{R}^2 \rightarrow \mathbb{R}$ . We choose to map to  $G_p$ , a sum of Gaussian functions which is defined by centering a Gaussian function at each point  $(x, y)$  in the persistence diagram and taking the sum of this set of functions. Taking a discretization of a subdomain of  $G_p$  defines a grid. An image can be created by computing the integral of  $G_p$  on each grid box, thus defining a matrix of pixel values. This “vectorization” of a persistence diagram brings to bear a host of new tools for comparing persistence diagrams, including all of the various metrics for measuring the distance between finite-dimensional vectors and a broad range of ML techniques.

Using topological features as a statistic for classification tasks is what motivates our development of persistence images. As is often done, we focus on sets of point-cloud data and use ML techniques to classify the point clouds by their topological features. We obtain PDs from data by the Vietoris-Rips filtration, which we then “vectorize” into a PI. While this is our focus, a PI could be used in any setting where a PD is used to represent topological information (*e.g.*, sub-level set persistence, etc.).

## 2 Background and Problem Statement

### 2.1 Homology and Data

Given a topological space  $\mathbb{M}$ , homology is an invariant that characterizes topological properties of the space. In particular, homology measures the number of connected components, loops, trapped volumes, and so on of a topological space, which can be used to distinguish distinct spaces from one another. More explicitly, the  $k$ -dimensional holes of a space generate a homology group,  $H_k(\mathbb{M})$ . The rank of this group is referred to as the  $k$ -th *Betti number*,  $\beta_k$ , and counts the number of  $k$ -dimensional holes of  $\mathbb{M}$ . For a comprehensive study of homology, see [10].

Data often comes equipped with one or more measures of internal dissimilarity. As such, datum is readily considered a point in a (pseudo)metric space – a member of a collection that may be rich with latent geometric content. One approach to extracting this content is to consider datum as vertices of a simplicial complex, with the presence of edges and higher order simplices determined by the relative dissimilarity of their singleton constituents. The homology of the simplicial complex is then determined. The resulting topological characterization depends crucially on a choice of scale. Persistent homology eliminates this choice by computing homology on a range of scales, recording the persistence of homological features across those scales. For details, see Appendix A and [2, 11, 12].

Two standard ways to represent persistent homology information are *barcodes* and *persistent diagrams* (PD). These tools indicate at which scale parameters topological features first appear (are ‘born’) and no longer remain (‘die’). In a barcode, a horizontal line segment begins at the birth of each feature and ends when the feature dies. At any given scale parameter, the Betti number  $\beta_k(\epsilon)$  is given by the number of bars that intersect a vertical line at  $\epsilon$ . On the other hand, a persistent diagram displays homological information as points in the Cartesian plane. The horizontal and vertical axes encode the birth and death parameters, respectively. Since all features die after they

are born, this is an embedding into the positive half plane above the diagonal. Two distinct features may have the same birth-death pair, so a PD is in fact a multiset of points<sup>1</sup>. Usually points near the diagonal are considered as noise while those further from the diagonal suggest more significant topological features.

## 2.2 Metric Spaces of PDs and Machine Learning

The space of PDs can be endowed with a metric, which has been studied in [9, 13, 14]. For instance, the *pth Wasserstein distance* defined between two PDs  $X$  and  $Y$  is given by

$$W_p(X, Y) := \inf_{\gamma: X \rightarrow Y} \left[ \sum_{x \in X} \|x - \gamma(x)\|_\infty^p \right]^{1/p},$$

where  $1 \leq p < \infty$  and  $\gamma$  ranges over bijections between  $X$  and  $Y$ . Another standard choice of distance between diagrams is  $W_\infty(X, Y) := \inf_{\gamma: X \rightarrow Y} \sup_{x \in X} \|x - \gamma(x)\|_\infty$ , referred to as the *bottleneck distance*.

The ability to compute distances between PDs allows one to complete ML tasks that rely only on the distance between objects, for example, some clustering algorithms. In this way, PDs can be thought of as a statistic for clustering the underlying topological spaces (or other objects). However, many other useful machine learning techniques require more than a pairwise distance matrix (*e.g.*, support vector machines, decision tree classification, and neural networks). Moreover, techniques such as feature selection and analysis by dimension reduction cannot be accomplished in this context either.

All of the ML tasks listed above become available if a PD can be represented by a vector. This is the primary motivation for developing an alternative, vector based, representation of a PD. Additionally, a vector representation would open the door to using  $p$ -norms (*e.g.* taxicab, Euclidean, infinity), angle based metrics, etc. These measures are significantly less computationally expensive as compared to the bottleneck distance (which has computational complexity  $O(n^3)$  where  $n$  is the number of birth-death pairs [1]). Thus, we are led to pose the following question:

**Problem Statement:** How can we represent a persistence diagram as a vector?

Our contribution to this question comes in the form of persistence images, which we discuss in § 4. Related approaches include [15, 16, 17, 18] which we briefly discuss in the next section.

## 3 Related Work

Encoding topological information in a way that enables a wider set of ML tools has been a recent area of interest in the TDA community. For instance, Bubenik develops the notion of a *persistence landscape*, a functional representation of a PD that lies in a Banach space, in [15]. In [16], Reininghaus *et al* develop a multi-scale kernel that allows for kernel-based ML algorithms such as kernel SVM and kernel PCA. Both of these approaches retain notions of stability while endowing persistence output with supplementary structure beyond a metric.

As an alternate approach, the authors of [17] create a sparse feature vector representation by binning a PD and counting the number of topological features existing in a ‘bin’ superimposed on the PD. These feature vectors are then understood as existing in a probability space. Like the approach discussed in [17], the authors of [18] focus on 0-dimensional homology in the context of

---

<sup>1</sup>We omit points that correspond to features with infinite persistence (*e.g.* the  $H_0$  feature corresponding to the connectedness of the complete simplicial complex).

sublevel set persistence, but in this case, the PD is transformed into a vector representation by computing the kernel density estimate on a uniform grid.

Our approach, developed concurrently and independently of those mentioned above, provides a representation of the information in a PD that allows for flexibility in its definition. We have chosen to place a Gaussian function at each point in the persistence diagram, but alternate functions could be used as well. Our representation also allows for suppressing points that are most likely noise while emphasizing true signal. In addition, distinct homology dimensions may be concatenated together and analyzed simultaneously. This vectorized representation allows for flexibility in the choice of metric and ML algorithm, which appears robust with regard to parameter selection.

## 4 Algorithm for Computing a Persistence Image

Out of a desire to maintain an interpretable connection to the original PD, it is natural to seek a way to directly vectorize the PD. One approach is to overlay an  $n \times m$  grid and simply count the points contained in each box of the grid to define a vector of length  $n \cdot m$ , similar to [17]. Unfortunately, this would produce a vector which is highly sensitive to the filtration step and the grid. Moreover, a fine grid would create a vector that is sparse, and consequently, the dot product between two different vectors is likely zero, which inhibits the use of meaningful angle-based metrics.

Assume that each point  $(b_x, b_y)$  in the PD  $\mathbf{B}$  is instead the center of a 2-dimensional normal distribution (or any appropriate distribution). By centering a Gaussian at each point and overlaying a grid, an image is defined by assigning each grid square a pixel value. Formally, we define  $I(p)$ , the value of each pixel  $p$  within an image, by the following equation:

$$I(p) = \iint_p \sum_{(b_x, b_y) \in \mathbf{B}} \frac{1}{2\pi\sigma_x\sigma_y} e^{-\frac{1}{2}\left(\frac{(x-b_x)^2}{\sigma_x^2} + \frac{(y-b_y)^2}{\sigma_y^2}\right)} dydx \quad (4.1)$$

where  $\sigma_x$  and  $\sigma_y$  are the variance of the Gaussian in the  $x$  and  $y$ -direction, respectively, and there is assumed to be no cross correlation. Recall that a PD is a multiset of points. Thus, we allow multiple Gaussians with the same center in the sum.

This pixel definition equally weights Gaussians defined on points close to the diagonal (which may be considered as noise) and far from the diagonal (which represent strong signal). In the case of noisy data, points in the original PD that are most likely noise may be so numerous that summing over all of the Gaussians centered at these points may wash out a small set of points in the PD that indicate a strong signal. In order to combat this effect of noise, we instead weight the contribution of each Gaussian based on the distance from the diagonal  $|\mathbf{b}| = b_y - b_x$ . This weighted image can be written as Equation 4.2,

$$I(p) = \iint_p \sum_{(b_x, b_y) \in \mathbf{B}} f(|\mathbf{b}|) \frac{1}{2\pi\sigma_x\sigma_y} e^{-\frac{1}{2}\left(\frac{(x-b_x)^2}{\sigma_x^2} + \frac{(y-b_y)^2}{\sigma_y^2}\right)} dydx \quad (4.2)$$

where the parameters are defined as in Equation 4.1, and  $f(|\mathbf{b}|)$  is a weighting function which depends on the distance from the diagonal. This weighting function could be chosen to suppress the effects of noise and amplify the signal. For example, a sigmoidal function or an exponential function would suppress points near the diagonal and give higher weights to the off-diagonal elements.

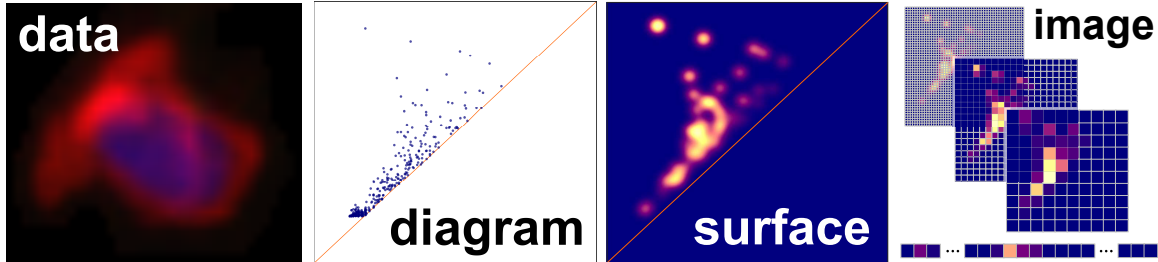


Figure 1: Algorithm pipeline to transform data into a persistence image.

#### 4.1 Parameters for Persistence Images:

There are three choices the user must make when generating a PI: the resolution, the distribution (and its associated parameters), and the weighting function.

**Resolution of the image:** The resolution of the PI corresponds to the grid being overlaid on the PD. We will see in § 5.3 that classification accuracy in the PI framework appears to be fairly robust to choice of resolution.

**The Distribution:** Our method requires the choice of a probability distribution which is associated to each of the points in the PD. In our implementation, we have chosen to center the same Gaussian distribution at each point, but this is not the only option. Flexibility in the choice of distribution is one distinguishing feature of our approach.

**The Weighting Function:** A weighting function could be used anytime there is believed to be noise in the data. Appropriate weighting functions ensure that the distributions centered at PD points closer to the diagonal (noise) are suppressed, while those further from the diagonal (signal) contribute more. We proceed using the weighting function,  $f(|\mathbf{b}|) = e^{M(|\mathbf{b}|)} - 1$ . This exponential weighting function was chosen because it lends itself to an intuitive way of selecting its parameter; setting the weight of the longest bar equal to one yields a simple formula for selecting  $M = \ln(2)/\mathbf{b}_{max}$  where  $\mathbf{b}_{max} = \max\{|\mathbf{b}| \text{ s.t. } \mathbf{b} \in \mathbf{B}\}$ . When the maximum bar length of the point clouds being compared differs, the maximum bar lengths across all diagrams should be used.

#### 4.2 Algorithm Pipeline

As an illustrative example we consider spectral and spatial information in  $\mathbb{R}^5$  from an immunofluorescent image of a circulating tumor cell [19] (‘data’ in Figure 1). Given a matrix of pairwise distances between points in the cloud, standard PH software can generate a PD (‘diagram’ in Figure 1). Next, a function is generated based on the selection of the probability distribution and weighting function (‘surface’ in Figure 1). Finally, based on the chosen resolution, a grid is overlaid and the value of each pixel is computed (Equation 4.2). Figure 1 shows PIs at different resolutions (labeled ‘image’). A reshaping of the image into a vector completes the algorithmic pipeline and provides a solution to the problem in § 2. Appendix B displays a variety of PIs.

### 5 Experiments on Simulated Data

The synthetic data set consists of point clouds in the unit cube sampled from six different topological spaces: the solid cube, a circle, a sphere, three clusters, three clusters within three clusters, and a torus. There are 25 sample point clouds consisting of 500 points for each type of space with two different levels of Gaussian random noise  $\eta = 0.05, 0.1$ . This data set was designed as one on which high classification accuracy is expected due to the known existence of differentiating topological

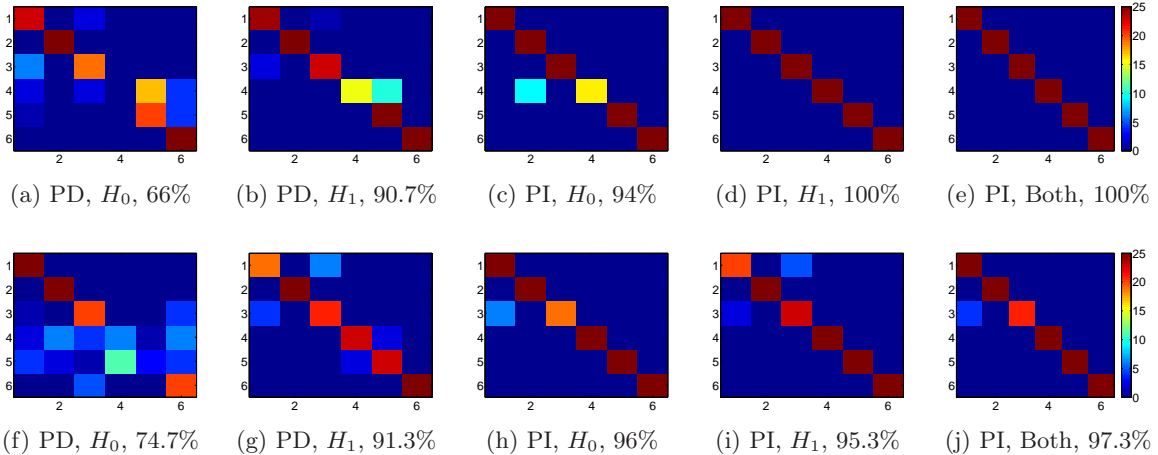


Figure 2: K-medoid confusion matrices (colored by number of samples classified) and corresponding overall accuracies of the synthetic data set sampled from 6 common topological spaces (solid cube, a circle, a sphere, three clusters, three clusters within three clusters, and a torus, respectively) with noise level (First Row)  $\eta = 0.05$  and (Second Row)  $\eta = 0.1$  for both the PD and PI frameworks with homological information labeled. ‘Both’ indicates concatenated  $H_0$  and  $H_1$  information.

features across the classes. We utilize this data for a variety of tasks: (1) comparing classification accuracy—using the clustering algorithm K-medoids [20, 21]—for the PD framework equipped with the bottleneck distance and the PI framework equipped with Euclidean distance, (2) using a linear support vector machine (SVM) as a classifier, a task which cannot be performed on PDs [22, 23], (3) describing the effect of parameter selection for PI generation on classification accuracy, and (4) analyzing this data set with *sparse* SVMs (SSVMs), which promote sparsity in the solution that can be used for topological feature selection [24, 25].

## 5.1 Comparison of K-medoids Classification

The iterative clustering algorithm K-medoids chooses an existing datum, represented by an index in a distance matrix, as the center of each cluster so that the distance between each point and the center with which it is identified is minimized [20, 21]. This algorithm takes as input a distance matrix together with the number of clusters  $K$  and can either be seeded with starting cluster centers or run unsupervised. As the space of PDs is a metric space under the bottleneck distance, K-medoids classification accuracy of PDs can be compared to that of PIs.

We compare K-medoids classification using PDs and PIs on  $H_0$  and  $H_1$  data sets<sup>2</sup>. Additionally, we can apply K-medoids simultaneously to  $H_0$  and  $H_1$  homological information by a concatenation of vectors. Comparison of concatenated PIs using a similarity measure analyzes the distance between respective homological dimensions; the same cannot be said of overlaying PDs of different homological dimension and using the bottleneck distance. This is a distinct difference between PIs and PDs.

<sup>2</sup>Pairwise bottleneck distance matrices were computed for the PDs corresponding to  $H_0$  and  $H_1$ . Pairwise Euclidean distance matrices were computed for the PIs corresponding to  $H_0$ ,  $H_1$ , and the concatenation of the  $H_0$  and  $H_1$  PI vectors. The PIs were computed using resolution  $\mathbf{R} = 50 \times 50$ , variance  $\sigma = 0.0951$ , and the weighting function  $f(|\mathbf{b}|) = e^{M(|\mathbf{b}|)} - 1$  with  $M = \ln(2)/\mathbf{b}_{max}$ . The K-medoids algorithm was initialized with starting centers to be one from each class.

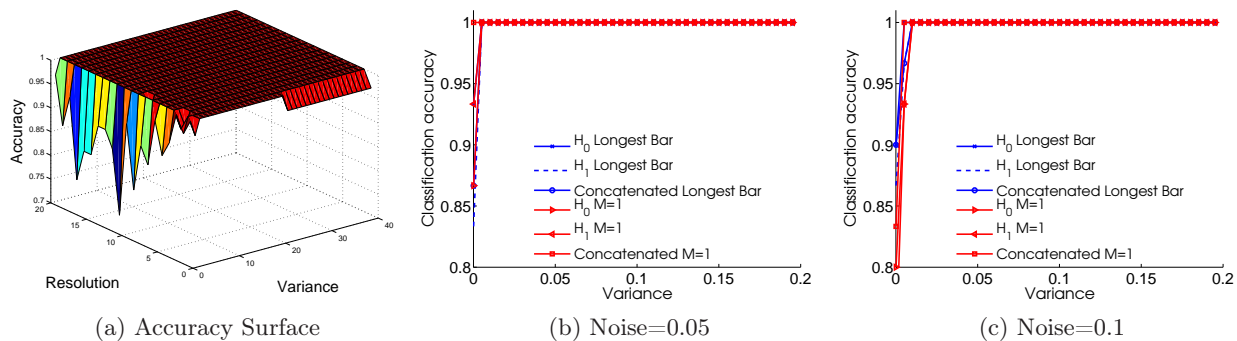


Figure 3: SVM classification accuracy plots of synthetic data set for Gaussian functions weighted by an exponential function with coefficient  $M = \ln(2)/\mathbf{b}_{max}$  (Longest bar) and  $M = 1$ . (a) Surface plot on  $H_0$  PIs for noise level  $\eta = 0.05$ . Observe that resolution has little to no effect on accuracy. (b) Accuracy as a function of variance for fixed resolution of  $50 \times 50$  for noise level  $\eta = 0.05$ . (c) Accuracy as a function of variance for fixed resolution of  $50 \times 50$  for noise level  $\eta = 0.1$ .

The first and second rows of Figure 2 display the overall classification accuracies (in %) and the images of the corresponding confusion matrices for noise level 0.05 and 0.1, respectively. The first two confusion matrices in each row correspond to the PD framework while the last three correspond to the PI framework. The same color map was used to generate each of these images, with blue representing 0 and red representing all 25 elements of a particular class. Recall the data consists of 25 samples of each of six different classes (the solid cube, a circle, a sphere, three clusters, three clusters within three clusters, and a torus), displayed in this order. Correctly labeled classes are displayed on the diagonal with errors elsewhere. The PD framework equipped with the bottleneck distance misclassified samples more often than the PI framework equipped with the Euclidean distance<sup>3</sup>.

In addition to superior classification accuracy using PIs, we also note a drastic improvement in computational time. To generate one pairwise bottleneck distance matrix for our synthetic data set took approximately  $1.9 \times 10^5$  seconds while generating a set of PIs and computing the pairwise Euclidean distance matrix for resolution  $50 \times 50$  took under 80 seconds for  $\eta = 0.05$  and under 300 seconds for  $\eta = 0.1$ .

## 5.2 SVM on PIs of Synthetic Data

As PIs are a vector representation, additional ML algorithms may be implemented on this data. We implement a linear  $\ell_2$ -norm regularized support vector machine (SVM) for classification [22, 23]. The SVM is a robust supervised binary classification method. For multiclass experiments, we adopt the one-against-one (OAO) SVM, *i.e.*, where a class label is assigned to a testing point based on majority voting over all possible pairwise binary SVM models between the classes. For a typical experiment, we partition data randomly into 80% for training and 20% for testing, *i.e.*, 20 PIs for training and 5 PIs for testing per class. We use the same set of PIs as for K-medoids classification. On the whole, classification accuracy was higher using SVMs than K-medoids, see Appendix C.

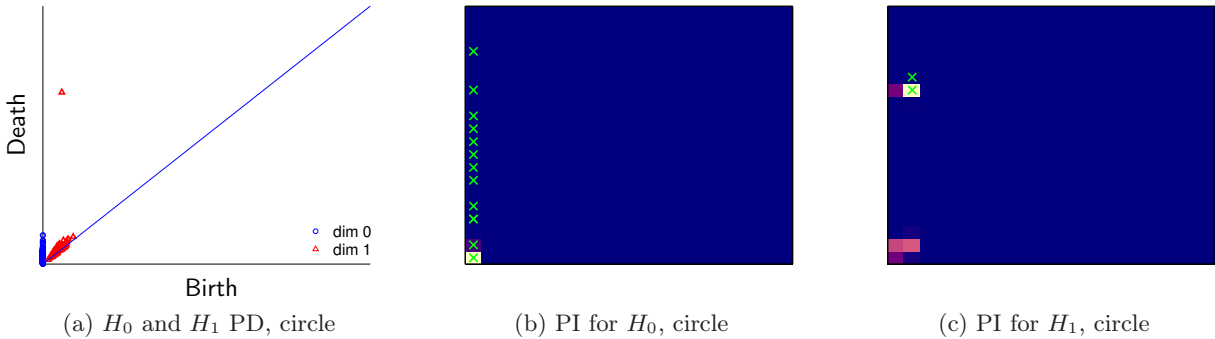


Figure 4: SSVM feature selection of a noisy circle, illustrated on one sample: (a)  $H_0$  and  $H_1$  PDs. (b) PI for dimension  $H_0$  and selected twelve features (17,16,13,12,7,9,11,4,20,14,10,19), marked by green crosses. (c) PI for dimension  $H_1$  and two selected features (26,27), marked by green crosses. Note that  $M = \ln(2)/\mathbf{b}_{max}$ ,  $\mathbf{R} = 20 \times 20$ , and variance  $\sigma = 0.0001$ , for noise level  $\eta = 0.05$ .

### 5.3 Effect of PI Parameter Selection

In any system that relies on multiple parameters, it is important to understand the effect of parameter values on the system. As such, we have completed a search of the space of parameters used to generate PIs and measured SVM classification accuracy as a function of the parameters. We explore 20 different resolutions<sup>4</sup>, use a Gaussian function with 40 different choices of variance<sup>5</sup>, and an exponential weighting function described in § 4.1 with two different choices of weighting coefficient<sup>6</sup>. For each set of parameters, we compute the classification accuracy on the two sets of noise levels for the homology dimensions  $H_0$  and  $H_1$  as well as the concatenation of the two. We observe that for a fixed variance, resolution has little to no effect on accuracy (see Figure 3a). Thus, in Figures 3b and 3c, we plot the classification accuracy using the SVM algorithm as a function of variance for the fixed resolution of  $50 \times 50$ . Although the plots are not constant, we see that there is a large set of variances which yield consistent accuracy for each homology type, and each parameter choice results in high accuracy. Note that it appears that classification of this data set is more robust to parameter selection using SVM than K-medoids, see Appendix D.

### 5.4 SSVM-Based Feature Selection

An  $\ell_1$ -norm regularized SVM (*a.k.a.* sparse SVM (SSVM)) simultaneously classifies data and selects input space features that contribute to the classification process [24, 25, 26]. Such a model can be used for reducing data dimension and removing redundant features. For example, using a one-against-all (OAA) approach on the sets of  $H_0$  and  $H_1$  PIs from the six class synthetic data set<sup>7</sup>, SSVM<sup>8</sup> results in 100% accuracy of six sparse models with indications of the discriminatory features. Feature selection is performed by retaining the features with non-zero SSVM weights, determined by magnitude comparison using weight ratios, for details see [27]. Figure 4 provides an example,

<sup>3</sup>Note that in unsupervised implementations of K-medoids—where starting centers are chosen randomly—this behavior was also observed

<sup>4</sup>ranging from  $5 \times 5$  to  $100 \times 100$  in increments of 5

<sup>5</sup>ranging from 0.0001 to 0.2 in increments of 0.005

<sup>6</sup> $M = 1$  and  $M = \ln(2)/\mathbf{b}_{max}$

<sup>7</sup>The PIs were generated using parameters  $M = \ln(2)/\mathbf{b}_{max}$ ,  $\mathbf{R} = 20 \times 20$ ,  $\sigma = 0.0001$ , and  $\eta = 0.05$

<sup>8</sup>using 80% of data for training and 20% for testing



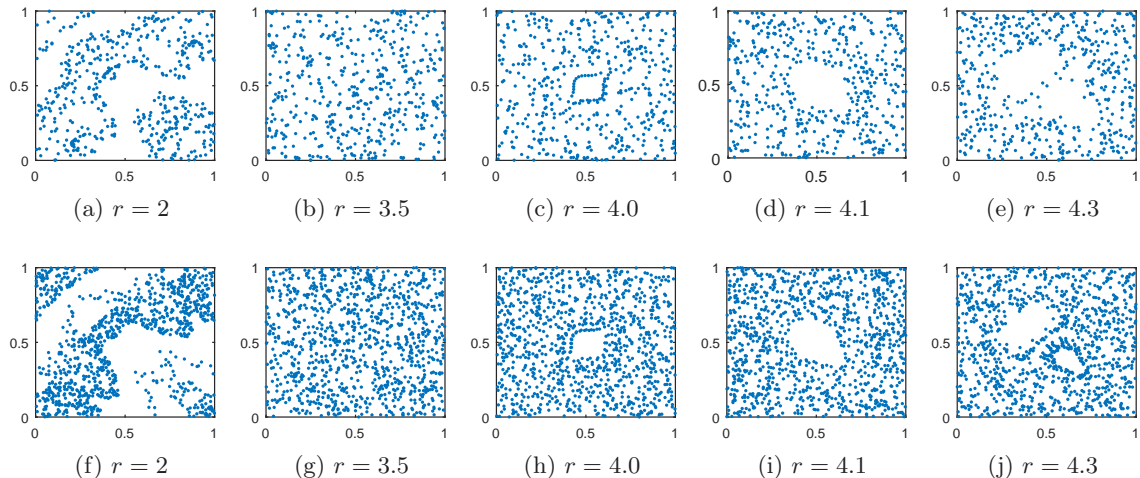


Figure 5: (First row) Examples of iterations of the Linked Twist Map, 500 points. (Second row) Examples of iterations of the Linked Twist Map, 1000 points.

indicating the features of a PI that discriminate circles from the other classes in the synthetic data set.

Feature selection produces highly interpretable results. For example, when performing classification using  $H_0$  PIs, a larger number of features are needed to separate circles from the remaining populations, which is reasonable since circles have no inherent  $H_0$  signature (highlighted in Figure 4b). Alternatively, the differentiating features that separate circles from the other classes using  $H_1$  PIs correspond to the region where strong  $H_1$  signal exists across all samples of a noisy circle (highlighted in Figure 4c). Similar conclusions can be drawn from the discriminatory features of others classes; see Appendix E for details on each of the six classes.

## 6 Classifying Orbits of the Linked Twist Map Using PIs

We approach a classification problem with data arising from the linked twist map, a discrete dynamical system modeling fluid flow. Hertzsch *et al.* [28] use the linked twist map to model flows in DNA microarrays with a particular interest in understanding turbulent mixing. The linked twist map is a Poincaré section of the continuous modeled flow arising from *eggbeater-type flow* [28] and is given by the coupled discrete dynamical system

$$x_{n+1} = x_n + ry_n(1 - y_n) \pmod{1}$$

$$y_{n+1} = y_n + rx_n(1 - x_n) \pmod{1},$$

where  $r$  is a positive parameter. The thrust of the paper of Hertzsch *et al.* is to design a system that mixes well. That is, as the map is iterated from an arbitrary initial condition, the set of points (the orbit) appears to fill the domain. This is the case for some regimes of the parameter  $r$ . However, for other parameter values, islands and complex structures form.

For this experiment, we choose a range of parameter values,  $r = 2.5, 3.5, 4.0, 4.1$  and  $4.3$ , which produce a variety of orbit patterns. For each parameter, 50 randomly-chosen initial conditions are selected, and either 500 or 1000 iterations of the linked twist map are used to generate point clouds in  $\mathbb{R}^2$ . The first and second rows of Figure 5 show examples of typical orbits generated for each

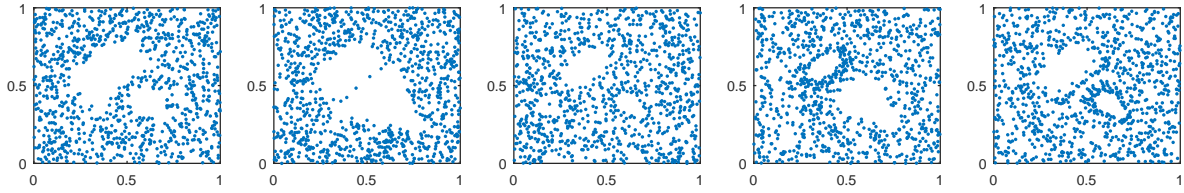


Figure 6: Examples of variations in a single parameter value of the Linked Twist Map,  $r = 4.3$ , 1000 points

parameter value of 500 and 1000 points, respectively. The goal is to classify the trials by parameter value. K-medoids is used to compare the PIs for all trials.<sup>9</sup>

For a large number of points (many thousands), the patterns formed by the orbits for various parameter values show only small visible variations in the patterns formed under perturbations of the initial condition. With only 500 points, there are more significant variations in the patterns produced because the full topology of the points has not had sufficient time to reveal itself. Figure 6 gives five examples of trials for  $r = 4.3$ , under 1000 iterations. The only variation between trials was a perturbation of the initial condition. Each example has two islands but there is enough variation between trials to cause classification to be difficult.  $H_1$  captures the presence and magnitude of holes in the data (islands) and using only the PIs generated from the  $H_1$  PDs allow us to capitalize on known structure in the data.

PIs arising from the first homology class,  $H_1$ , are used for classification purposes by means of K-medoids. Including all 5 parameters yields classification rates of 68% for 500 points and 71% for 1000 points. Largely the errors were instances of  $r = 3.5$  classified as  $r = 4.0$ . This occurs because when  $r = 4.0$  the tight island in the center can be quite small for some initial conditions, and for  $r = 3.5$  occasionally voids between points will appear when there are 1000 points or fewer. Perturbation of the initial condition can cause a significant change in the structure of the orbit, particularly for  $r = 4.1$ . Occasionally a line of points will cross the island formed in the center, causing the topology to resemble that of the typical points from  $r = 4.3$ . Consequently, the misclassification of examples from  $r = 4.1$  and  $r = 4.3$  is reasonable.

When the problematic parameter values ( $r = 3.5$  and  $r = 4.1$ ) are omitted, classification significantly improves. The set of data with 1000 points is classified with 96% accuracy, and the set with 500 points is classified with a 92 % accuracy. Note that in this context, 500 points is a relatively low number, where some of the complex structures are in the early stages of formation and are often difficult to distinguish. Even on a small number of points, PIs are capable of detecting topological differences and highlight the feature that varies with parameter choices. This application—a brief example of the utility of PIs in classification of data from dynamical systems and modeling real-world phenomena—provides a promising direction for further applications of PIs.

## 7 Conclusions

Persistence images provide a method for vectorization of the topological characteristics captured by a persistence diagram. Additionally, PIs provide wider access to a variety of machine learning tools that can be used to multiple ends. It is curious to note that although these PIs are not

<sup>9</sup>We use  $\mathbf{R} = 20 \times 20$ , a Gaussian with variance  $\sigma = 0.001$ , and exponential weighting function with coefficient  $M = 1$  to generate the PIs. These parameters were chosen after a preliminary parameter search and classification effort.

stable in their current form, they produce high classification accuracy. If one is concerned with the stability of the representation, it would be possible to join our discretization method with the function representation presented in [16] for which a type of stability has been proven.

We have shown that PIs yield higher classification accuracy than PDs on sampled data of common topological spaces, at multiple noise levels, via K-medoids. Moreover, a significant reduction in computational time to generate the bottleneck distance matrices versus generating a set of PIs and Euclidean distance matrices is achieved. We have also shown that classification accuracy of PIs seems fairly robust to parameter selection for a simulated data set. Through the introduction of PIs we have access to a wider selection of machine learning tools, like SVM, which can produce higher classification rates and SSVM, which can be used for feature selection. Due to the interpretable mapping between PDs and PIs, features selected in a PI directly correlate with regions in a PD. Although not explored in this paper, the vectorization allows for distance matrices based on a wide variety of dissimilarity measures which could result in further accuracy improvements. The flexibility of defining PIs allows for customization tailored to a variety of real world data sets.

**Acknowledgements:** We would like to acknowledge the research group of Paul Bendich at Duke University for allowing us access to a PH package which greatly reduced computational time and made analysis of large point clouds feasible. This code can be accessed via GitLab after submitting a request to Paul Bendich.

This research is partially supported by the National Science Foundation under Grants No. DMS-1228308, DMS-1322508, NSF DMS-1115668, and NSF DMS-1412674 as well as the DOD-USAF under Award Number FA9550-12-1-0408. Any opinions, findings, and conclusions or recommendations expressed in this material are those of the authors and do not necessarily reflect the views of the National Science Foundation or the United States Air Force.

## References

- [1] Herbert Edelsbrunner and John L. Harer. *Computational Topology, An Introduction*. American Mathematical Society, 2010.
- [2] Robert Ghrist. Barcodes: the persistent topology of data. *Bulletin of the American Mathematical Society*, 45(1):61–75, 2008.
- [3] Kyle Heath, Natasha Gelfand, Maks Ovsjanikov, Mridul Aanjaneya, and Leonidas J Guibas. Image webs: Computing and exploiting connectivity in image collections. In *Computer Vision and Pattern Recognition (CVPR), 2010 IEEE Conference on*, pages 3432–3439. IEEE, 2010.
- [4] Jose A Perea and John Harer. Sliding windows and persistence: An application of topological methods to signal analysis. *Foundations of Computational Mathematics*, pages 1–40, 2013.
- [5] Yu Dabaghian, Facundo Memoli, L Frank, and Gunnar Carlsson. A topological paradigm for hippocampal spatial map formation using persistent homology. *PLoS computational biology*, 8(8):e1002581, 2012.
- [6] Moo K Chung, Peter Bubenik, and Peter T Kim. Persistence diagrams of cortical surface data. In *Information Processing in Medical Imaging*, pages 386–397. Springer, 2009.
- [7] Gurjeet Singh, Facundo Memoli, Tigran Ishkhanov, Guillermo Sapiro, Gunnar Carlsson, and Dario L Ringach. Topological analysis of population activity in visual cortex. *Journal of vision*, 8(8):11, 2008.

- [8] Chad M. Topaz, Lori Ziegelmeier, and Tom Halverson. Topological data analysis of biological aggregation models. *PLoS ONE*, 10(5):e0126383, 05 2015. doi: 10.1371/journal.pone.0126383. URL <http://dx.doi.org/10.1371%2Fjournal.pone.0126383>.
- [9] Yuriy Mileyko, Sayan Mukherjee, and John Harer. Probability measures on the space of persistence diagrams. *Inverse Problems*, 27(12):124007, 2011.
- [10] Allen Hatcher. *Algebraic topology*. Cambridge University Press, 2002.
- [11] Gunnar Carlsson. Topology and data. *Bulletin of the American Mathematical Society*, 46(2):255–308, 2009.
- [12] Herbert Edelsbrunner and John Harer. Persistent homology - a survey. *Contemporary mathematics*, 453:257–282, 2008.
- [13] David Cohen-Steiner, Herbert Edelsbrunner, and John Harer. Stability of persistence diagrams. *Discrete & Computational Geometry*, 37(1):103–120, 2007.
- [14] Elizabeth Munch, Katharine Turner, Paul Bendich, Sayan Mukherjee, Jonathan Mattingly, and John Harer. Probabilistic Fréchet means for time varying persistence diagrams. *Electron. J. Statist.*, 9:1173–1204, 2015. doi: 10.1214/15-EJS1030. URL <http://dx.doi.org/10.1214/15-EJS1030>.
- [15] Peter Bubenik. Statistical topology using persistence landscapes. *arXiv preprint arXiv:1207.6437*, 2012.
- [16] Jan Reininghaus, Stefan Huber, Ulrich Bauer, and Roland Kwitt. A stable multi-scale kernel for topological machine learning. *arXiv preprint arXiv:1412.6821*, 2014.
- [17] Paul Bendich, Sang Chin, Jesse Clarke, Jonathan deSena, John Harer, Elizabeth Munch, Andrew Newman, David Porter, David Rouse, Nate Strawn, et al. Topological and statistical behavior classifiers for tracking applications. *arXiv preprint arXiv:1406.0214*, 2014.
- [18] Deepti Pachauri, Christian Hinrichs, Moo K Chung, Sterling C Johnson, and Vikas Singh. Topology-based kernels with application to inference problems in Alzheimer’s disease. *Medical Imaging, IEEE Transactions on*, 30(10):1760–1770, 2011.
- [19] Tegan Emerson, Michael Kirby, Kelly Bethel, Anand Kolatkar, Madelyn Luttgen, Stephen O’Hara, Paul Newton, and Peter Kuhn. Fourier-ring descriptor to characterize rare circulating cells from images generated using immunofluorescence microscopy. *Computerized Medical Imaging and Graphics*, 40:70–87, 2015.
- [20] Leonard Kaufman and Peter Rousseeuw. *Clustering by means of medoids*. North-Holland, 1987.
- [21] Hae-Sang Park and Chi-Hyuck Jun. A simple and fast algorithm for k-medoids clustering. *Expert Systems with Applications*, 36(2):3336–3341, 2009.
- [22] Vladimir N. Vapnik. *The nature of statistical learning theory*. Springer-Verlag New York, Inc., New York, NY, USA, 1995. ISBN 0-387-94559-8.
- [23] Christopher J. C. Burges. A tutorial on support vector machines for pattern recognition. *Data Mining and Knowledge Discovery*, 2:121–167, 1998.

- [24] Paul S. Bradley and Olvi L. Mangasarian. Feature selection via concave minimization and support vector machines. In *Machine Learning Proceedings of the Fifteenth International Conference*, ICML '98, pages 82–90. Morgan Kaufmann, 1998.
- [25] Ji Zhu, Saharon Rosset, Trevor Hastie, and Rob Tibshirani. 1-norm support vector machines. *Neural Information Processing Systems*, (16), 2003.
- [26] Li Zhang and Weida Zhou. On the sparseness of 1-norm support vector machines. *Neural networks : the official journal of the International Neural Network Society*, 23(3):373–85, April 2010.
- [27] Sofya Chepushtanova, Christopher Gittins, and Michael Kirby. Band selection in hyperspectral imagery using sparse support vector machines. In *Proceedings SPIE DSS 2014*, volume 9088, pages 90881F–90881F15, 2014.
- [28] Jan-Martin Hertzsch, Rob Sturman, and Stephen Wiggins. DNA microarrays: Design principles for maximizing ergodic, chaotic mixing. *Small*, 3(2):202–218, 2007. ISSN 1613-6829. doi: 10.1002/sml.200600361. URL <http://dx.doi.org/10.1002/sm11.200600361>.

## A Homology and Data

Given a topological space  $\mathbb{M}$ , homology is an invariant that characterizes topological properties of the space. In particular, homology measures the number of connected components, loops, trapped volumes, and so on of a topological space, which can be used to distinguish distinct spaces from one another. More explicitly, the  $k$ -dimensional holes of a space generate a homology group,  $H_k(\mathbb{M})$ . The rank of this group is referred to as the  $k$ -th Betti number,  $\beta_k$ , and counts the number of  $k$ -dimensional holes of  $\mathbb{M}$ . For a comprehensive study of homology, see [10].

Given a point cloud of data, homology is computed by first constructing connections between nearby data points and then computing homology on the topological space formed by these connections, a simplicial complex. The notion of ‘near’, and hence, the topological features, can change at a variety of scales. Thus, we compute homology at many scales and observe which topological features persist across those scales. This is called persistent homology, which is discussed further in § A.2. For additional details, see [2, 11, 12]

### A.1 Simplicial Complexes and Homology

A *simplicial complex* is a global object built from a discrete set of  $N$  points. It is a topological space  $S$  consisting of points (0-simplices), edges (1-simplices), triangles (2-simplices), tetrahedrons (3-simplices), and higher dimensional  $k$ -simplices, such that (1) if  $\sigma$  is a simplex in  $S$  then  $S$  contains all lower-dimensional simplices of  $\sigma$  and (2) the non-empty intersection of any two simplices in  $S$  is a simplex in  $S$ . While the topological characteristics of a simplicial complex can be interesting in their own right, often a simplicial complex is used to approximate another topological space  $\mathbb{M}$  and thus, to approximate the topological characteristics of  $\mathbb{M}$ .

There are a variety of methods to build simplicial complexes from a point cloud of data, but we restrict our focus on the *Vietoris-Rips complex* for its computational tractability [2]. This complex relies on the data points themselves and on an  $N \times N$  pairwise distance matrix. For a given scale parameter  $\epsilon$ , the simplicial complex  $S_\epsilon$  is constructed by including the data points as 0-simplices and for every collection of  $k + 1$  points whose pairwise distance is less than  $\epsilon$ , including a  $k$ -simplex.

To a simplicial complex, one can associate a chain complex of vector spaces over a field  $\mathbb{F}$  (often, in practice, a finite field  $\mathbb{Z}_p$  for small prime  $p$ ),

$$\cdots \rightarrow C_{k+1} \xrightarrow{\delta_{k+1}} C_k \xrightarrow{\delta_k} C_{k-1} \cdots$$

The  $k$ -simplices form a basis for the vector space  $C_k$ , which consists of linear combinations of the  $k$ -simplices over  $\mathbb{F}$ . The linear map  $\delta_k : C_k \rightarrow C_{k-1}$ , known as the *boundary operator*, maps a  $k$ -simplex to a sum of its  $k - 1$ -faces, its boundary. More formally, if  $[v_0, v_1, \dots, v_k]$  is a  $k$ -simplex, the boundary map is defined by

$$\delta_k([v_0, v_1, \dots, v_k]) = \sum_{i=0}^k (-1)^i [v_0, \dots, \hat{v}_i, \dots, v_k]$$

where  $[v_0, \dots, \hat{v}_i, \dots, v_k]$  is the  $(k - 1)$ -simplex obtained from  $[v_0, \dots, v_k]$  by removing vertex  $v_i$ .

We define two subspaces of  $C_k$  by the kernel and image of the boundary operators:  $Z_k = \ker(\delta_k)$ , known as the  $k$ -cycles, and  $B_k = \text{im}(\delta_{k+1}) = \delta_{k+1}(C_{k+1})$ , known as the  $k$ -boundaries. The boundary operator satisfies the property  $\delta_k \circ \delta_{k+1} = 0$ . Thus, the subspace of boundaries  $B_k \subseteq Z_k$ , the subspace of cycles.

Homology seeks to uncover an equivalence class of cycles that enclose a  $k$ -dimensional hole—that is, cycles which are not also boundaries of  $k$ -simplices. To this end, the  $k$ th order homology is defined as  $H_k(S_\epsilon) = Z_k/B_k$ , a quotient of vector spaces. The  $k$ th Betti number is the dimension of this vector space  $\beta_k = \dim(H_k(S_\epsilon))$  which counts the number of independent holes of dimension  $k$ . More explicitly,  $\beta_0$  counts the number of connected components,  $\beta_1$  the number of loops,  $\beta_2$  the number of trapped volumes, and so on. Betti numbers are a topological invariant, meaning that topologically equivalent spaces have the same Betti number.

## A.2 Persistent Homology and Data

To uncover the topological characteristics of a point cloud, one follows the process described above; however, the choice of  $\epsilon$  is often not apparent. Selecting  $\epsilon$  too small results in a topological space with the same homology as a collection of points, but selecting  $\epsilon$  too large results in a topological space that is equivalent to a single point. One solution to this problem is to consider a collection of nested simplicial complexes indexed by parameter  $\epsilon$ . That is, if  $\epsilon_1 \leq \epsilon_2 \leq \dots$ , then the corresponding simplicial complexes satisfy  $S_{\epsilon_1} \subseteq S_{\epsilon_2} \subseteq \dots$ . As  $\epsilon$  varies, the topological characteristics of the simplicial complexes change. Persistent homology tracks the topological features over a range of values of  $\epsilon$ . Those features which persist over a larger range are considered to be true topological characteristics while short-lived features are often considered as noise.

Two standard ways to represent persistent homology information are *barcodes* and *persistent diagrams* (PD). These tools indicate at which parameters  $\epsilon$  topological features first appear (are ‘born’) and when they no longer remain (‘die’). In a barcode, a horizontal line segment begins at the birth of each feature and ceases to exist when the feature dies. There is no inherent ordering of the bars in the barcode. At any given  $\epsilon$ , the Betti number  $\beta_k(\epsilon)$  is the number of bars that intersect the vertical line through  $\epsilon$ . As previously mentioned, bars which persist over large scales represent topological features while short-lived bars are often considered as noise. A persistent diagram, on the other hand, displays homological information by embedding it into the Cartesian plane. The horizontal and vertical axes encode the birth and death parameters, respectively. Since all components die after they are born, this is an embedding into the upper half plane, above the diagonal  $\Delta = \{(x, x) \in \mathbb{R}^2 | x \in \mathbb{R}\}$ . Features may be born and die simultaneously, so this creates a multiset with infinitely many copies of the diagonal. Points near the diagonal are considered as

noise while those further from the diagonal signal topological features. There is a distinct barcode and PD for each homology space  $H_k$ .

## B Examples of Persistence Images

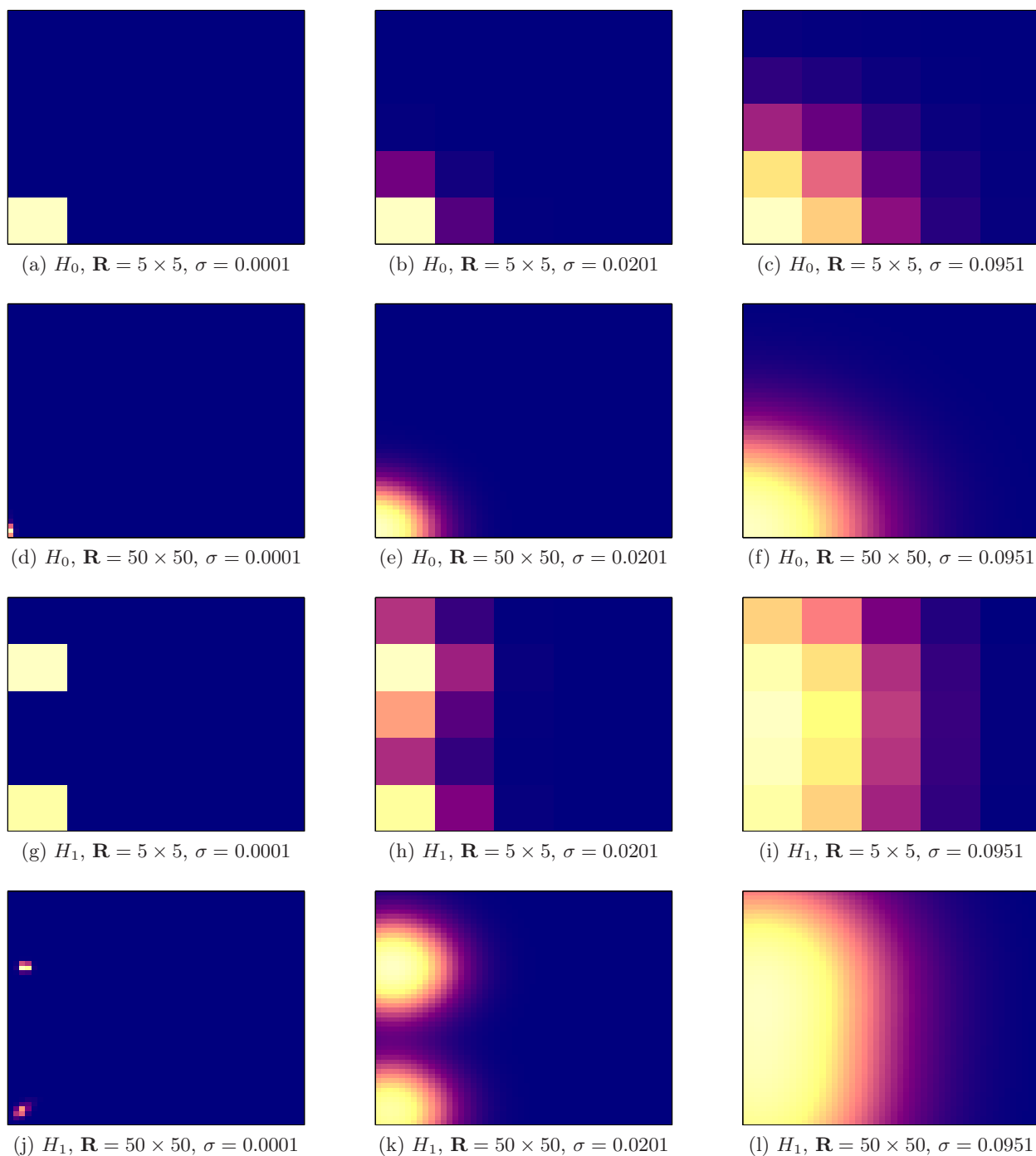


Figure 7: Examples of PIs for homology dimension  $H_0$  and  $H_1$  arising from a noisy circle for a variety of resolutions  $\mathbf{R}$ , a Gaussian distribution with variance  $\sigma$ , and weighting function  $f(|\mathbf{b}|) = e^{M(|\mathbf{b}|)} - 1$  with  $M = \ln(2)/\mathbf{b}_{max}$ .



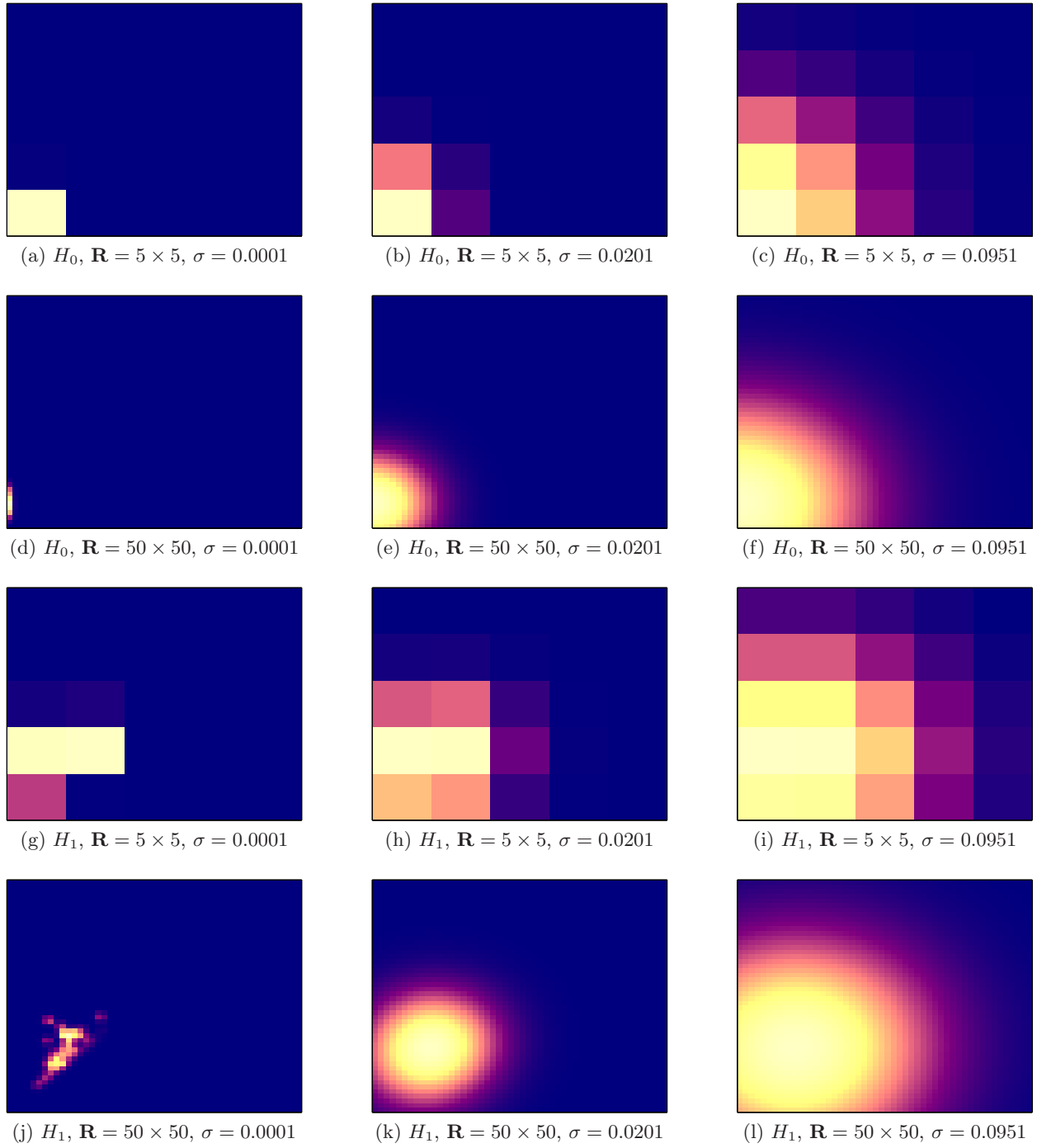


Figure 8: Examples of PIs for homology dimension  $H_0$  and  $H_1$  arising from a noisy torus for a variety of resolutions  $\mathbf{R}$ , a Gaussian distribution with variance  $\sigma$ , and weighting function  $f(|\mathbf{b}|) = e^{M(|\mathbf{b}|)} - 1$ , with  $M = \ln(2)/\mathbf{b}_{max}$ .

## C SVM on PIs of Synthetic Data Results

The synthetic data set consists of point clouds existing within the unit cube sampled from six different topological spaces: the solid cube, a circle, a sphere, three clusters, three clusters within three clusters, and a torus. There are 25 sample point clouds consisting of 500 points for each type of space with two different levels of Gaussian random noise  $\eta = 0.05, 0.1$ .

We implement a linear  $\ell_2$ -norm regularized support vector machine (SVM) for classification on this data [22, 23]. An SVM is a supervised binary classifier, and for multiclass experiments we adopt the one-against-one approach with majority voting. For a typical experiment, we partition data randomly into 80% for training and 20% for testing, *i.e.*, 20 PIs for training and 5 PIs for testing per class. We use the same set of PIs as for K-medoid classification with resolution  $\mathbf{R}$  is  $50 \times 50$ , variance  $\sigma = 0.0951$ , and the weighting function was chosen as the exponential  $f(|\mathbf{b}|) = e^{M(|\mathbf{b}|)} - 1$  with  $M = \ln(2)/\mathbf{b}_{max}$ .

The confusion matrices for the experiment conducted using the  $H_0$ ,  $H_1$ , and concatenated PIs with noise level 0.05, are shown in the first row of Figure 9, while similar experiments for the data with noise level 0.1 are shown in the second row. The same color map was used to generate each of these images, with blue representing 0 and red representing the 5 elements in each test class. Correctly labeled classes are displayed on the diagonal with errors elsewhere. The PIs provide an excellent framework for SVM classification for this data set, with only one element misclassified across all homology representations. Note that without PIs we would be unable to utilize a linear SVM classifier on this data.

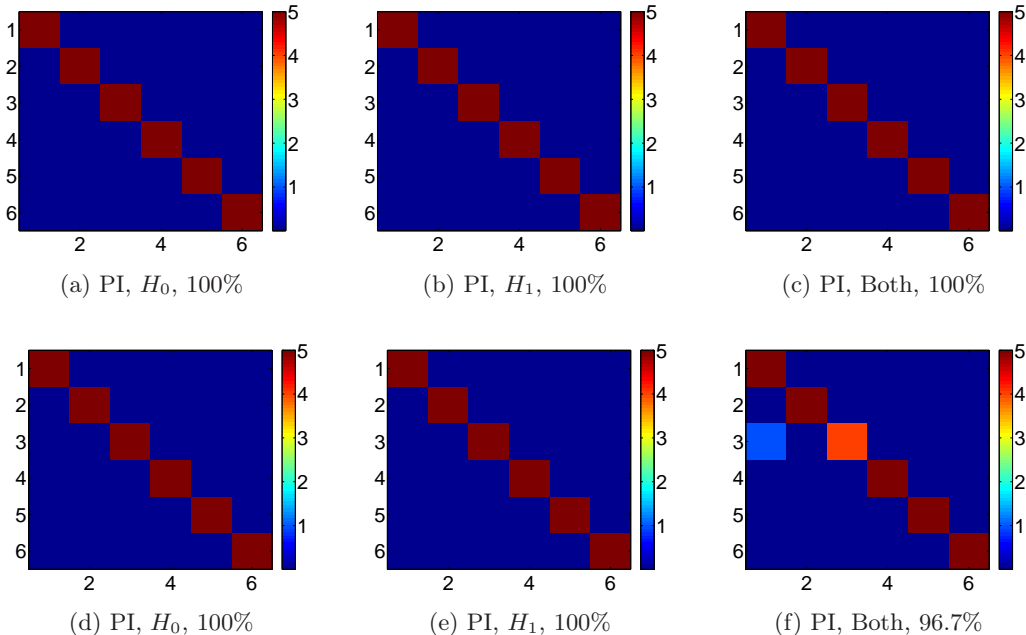


Figure 9: SVM confusion matrices (colored by number of samples classified) and corresponding overall accuracies of the synthetic data set of 6 common topological spaces (solid cube, a circle, a sphere, three clusters, three clusters within three clusters, and a torus, respectively) with noise level (First Row)  $\eta = 0.05$  and (Second Row)  $\eta = 0.1$  in the PI framework with homological information labeled. ‘Both’ indicates concatenated  $H_0$  and  $H_1$  information.

## D Effect of PI Parameter Selection Using K-medoids

In Section §5.3, we completed a parameter space search on PIs generated from the synthetic data set, measuring the SVM classification accuracy as a function of the parameters. In this section, we consider the same parameter space search using the K-medoid algorithm to classify. We explore 20 different resolutions ranging from  $5 \times 5$  to  $100 \times 100$  in increments of 5. We select a Gaussian function with 40 different choices of variance ranging from 0.0001 to 0.2 in increments of 0.005 weighted by the exponential function described in Section 4.1 with two different choices of weighting coefficient  $M = 1$  and  $M = \ln(2)/\mathbf{b}_{max}$  (which we denote as longest bar). For each set of parameters, we compute the classification accuracy on the two sets of noise levels for the homology dimensions  $H_0$  and  $H_1$  as well as the concatenation of the two. We observe that for a fixed variance, resolution has little to no effect on accuracy, see for instance, Figure 10a. Thus, in Figures 10b and 10c, we plot the classification accuracy of the noise levels 0.05 and 0.1 using the K-medoids algorithm as a function of variance for the fixed resolution of  $50 \times 50$ . Although the plots are not constant, we see that there is a large set of variances which yield consistent accuracy for each homology type, particularly when variance is not too large. Variance in the Gaussian is indirectly related to the level of certainty in the true start and death time of the topological features. As the variance increases, accuracy may fall. Furthermore, we see a more pronounced effect of variance on accuracy based on  $H_0$  features over either  $H_1$  or concatenated PIs. Note that it appears that SVM classification is more robust to parameter selection than K-medoids for this data set.

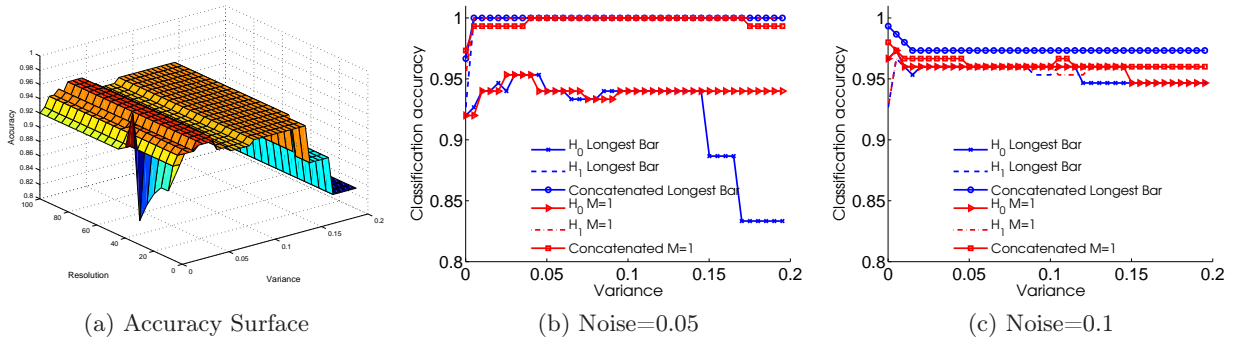


Figure 10: K-medoids classification accuracy plots of synthetic data set for Gaussian functions weighted by an exponential function with coefficient  $M = \ln(2)/\mathbf{b}_{max}$  (Longest bar) and  $M = 1$ . (a) Surface plot on  $H_0$  PIs for noise level  $\eta = 0.05$ . Observe that resolution has little to no effect on accuracy. (b) Accuracy as a function of variance for fixed resolution of  $50 \times 50$  for noise level  $\eta = 0.05$ . (c) Accuracy as a function of variance for fixed resolution of  $50 \times 50$  for noise level  $\eta = 0.1$ .

## E SSVM-based Feature Selection

We perform feature selection using one-against-all (OAA) SSVM on the six classes of synthetic data. The PIs used in the experiments were generated from the  $H_0$  and  $H_1$  PDs, with the parameter choices of  $M = \ln(2)/\mathbf{b}_{max}$ ,  $\mathbf{R} = 20 \times 20$ , variance  $\sigma = 0.0001$ , and noise level  $\eta = 0.05$ . Note that because of the resolution parameter choice of  $\mathbf{R} = 20 \times 20$ , each PI is a 400-dimensional vector. We trained two OAA SSVM models, one for PIs of dimension  $H_0$ , and one for PIs of dimension  $H_1$ . In both experiments, we used 80% of data for training and 20% for testing and obtained 100% overall accuracy. Feature selection was performed by retaining the features with non-zero SSVM

Table 1: OAA SSVM-based feature selection results for six classes of the synthetic data set. Discriminatory pixel indices of the vectorized PI in classifying each class from all other classes are listed below, ordered by weight magnitude.

Classes	PIs for $H_0$	PIs for $H_1$
Solid cubes	17,18,19	76,57,77,56
Circles	17,16,13,12,7,9,11,4,20,14,10,19	27,26
Spheres	18,19	58,76,77,56
3 Clusters	17,13,18,16,9,7,12,14,19,11,20,4,10	20,19
3 Clusters within 3 Clusters	20,19	19,57,39,76,95,94,75
Tori	17	95,75,74,57

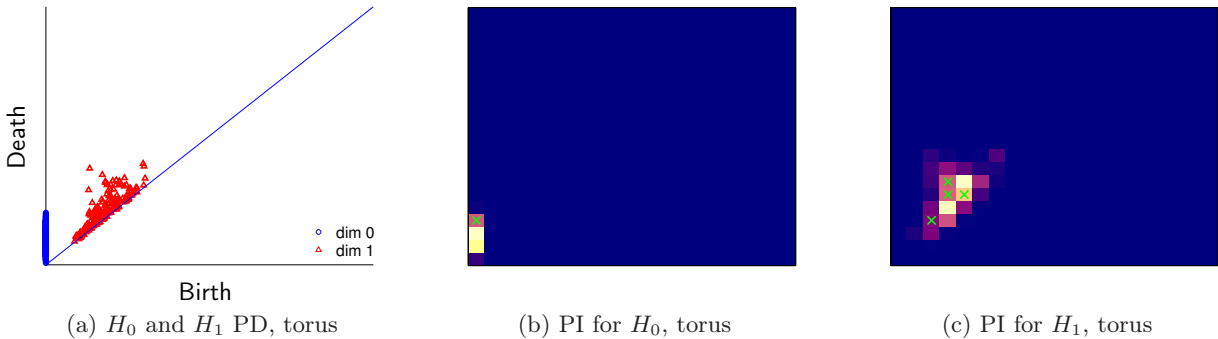


Figure 11: Examples of SSVM feature selection for a noisy torus: (a)  $H_0$  and  $H_1$  PDs. (b) PI for dimension  $H_0$  and one selected feature 17, marked by a green cross. (c) PI for dimension  $H_1$  and four selected features (95,75,74,57), marked by green crosses. Note that  $M = \ln(2)/\mathbf{b}_{max}$ ,  $\mathbf{R} = 20 \times 20$ , and variance  $\sigma = 0.0001$ , for noise level  $\eta = 0.05$ .

weights, determined by magnitude comparison using weight ratios [27]. The resulting six sparse models contain subsets of discriminatory features for each class, for both  $H_0$  and  $H_1$  dimensions. Note that one can use only these selected features for classification without loss in accuracy. These features correspond to discriminatory pixels in the persistence images.

Table 1 contains the features (indices of pixels in the vectorized PIs) selected by OAA SSVM that discriminate each class from all the others. All  $H_0$  topological features are born at scale  $\epsilon = 0$  in the PD. This corresponds precisely to the leftmost column in the PI with vectorized pixel values 1 (top left) and 20 (bottom left). The  $H_0$  features selected by OAA SSVM are all located in this first column of the PI. The  $H_1$  features selected by OAA SSVM of the PIs also correspond to regions of interest in the PD. We further illustrate the contribution of feature selection in Figure 11 by considering one sample of the noisy torus and the corresponding persistence images for  $H_0$  and  $H_1$  dimensions (see also Figure 4 in Section 5.4 for a noisy circle example). To separate the class of tori from all the rest using PIs for  $H_0$  dimension, only one feature (17) out of 400 is needed, see a corresponding pixel marked by a green cross in the persistence image in Figure 11b. In the experiment of the tori-versus-rest for  $H_1$  dimension, four features (95,75,74,57) discriminate the class of tori from the rest, see Figure 11c. Note that the selected features in the  $H_1$  PI indicate the regions in the PD (Figure 11a) with the  $H_1$  signals that differentiate a torus from the rest.